2000-04

Wave optics simulation of atmospheric turbulence and reflective speckle effects in CO2 lidar

Nelson, Douglas H.

Wave optics simulation of atmospheric turbulence and reflective speckle effects in CO_2 lidar

Douglas H. Nelson, Donald L. Walters, Edward P. MacKerrow, Mark J. Schmitt, Charles R. Quick, William M. Porch, and Roger R. Petrin

Laser speckle can influence lidar measurements from a diffuse hard target. Atmospheric optical turbulence will also affect the lidar return signal. We present a numerical simulation that models the propagation of a lidar beam and accounts for both reflective speckle and atmospheric turbulence effects. Our simulation is based on implementing a Huygens–Fresnel approximation to laser propagation. A series of phase screens, with the appropriate atmospheric statistical characteristics, are used to simulate the effect of atmospheric turbulence. A single random phase screen is used to simulate scattering of the entire beam from a rough surface. We compare the output of our numerical model with separate CO_2 lidar measurements of atmospheric turbulence and reflective speckle. We also compare the output of our model with separate analytical predictions for atmospheric turbulence and reflective speckle. Good agreement was found between the model and the experimental data. Good agreement was also found with analytical predictions. Finally, we present results of a simulation of the combined effects on a finite-aperture lidar system that are qualitatively consistent with previous experimental observations of increasing rms noise with increasing turbulence level. © 2000 Optical Society of America

OCIS codes: 010.1130, 030.6140, 010.3640.

1. Introduction

Lidar is the subject of a vast literature describing the advances that have occurred over the past three decades.[1–6] Long-range CO_2 lidar is of interest for many reasons including the identification of natural and man-made gaseous constituents, ground-cover identification and mapping, and atmospheric characterization.[5,7,8] In these lidar systems, the beam propagates several kilometers through the atmosphere. To enhance the lidar return signal, the lidar beam is often reflected from a topographic or other diffuse hard target back to the transmitter and receiver, where the return signal is detected.[9] In effluent detection and monitoring applications that use diffuse hard-target reflections, the path-integrated properties of chemical concentration are measured instead of the range-resolved concentration found with aerosol backscatter techniques.[10,11]

The geometry for a diffuse hard-target reflection scheme is shown in Fig. 1. As the laser beam propagates toward the target, density fluctuations in the atmosphere cause phase distortions in the transverse electric field distribution. By the time the laser beam reaches the target, its spatial intensity distribution has been modified compared with what would be observed in propagating through a vacuum. At the target, light is scattered backward toward the transmitter. The light scattered back toward the transmitter and receiver passes through essentially the same turbulent atmosphere that modified the outgoing beam (because the atmosphere is considered frozen during the transit time of the pulse for our typical lidar geometries). The return signal amplitude will be reduced by any chemical absorbers in the path in a manner consistent with Beer's law. Absorption will also occur from natural atmospheric constituents.

The atmosphere alone can introduce variations in the measured return signal. Figure 1 illustrates the degrading effect that atmospheric optical turbulence has on the spatial profile of the laser beam. These degradations result from the variations in the phase

When this research was performed, D. H. Nelson, E. P. MacKerrow, M. J. Schmitt, C. R. Quick, W. M. Porch, and R. R. Petrin (rrp@lanl.gov) were with the Los Alamos National Laboratory, CST-1/MS E543, P.O. Box 1663, Los Alamos, New Mexico 87545. D. H. Nelson (dnelson1@notes.west.raytheon.com) is now with Raytheon, Building 801, MS E6A, P.O. Box 11337, Tucson, Arizona 85734-1337. D. L. Walters is with the Department of Physics, Naval Postgraduate School, 1 University Circle, Monterey, California 93943-5001.

Received 14 April 1999; revised manuscript received 5 October 1999.

0003-6935/00/121857-15$15.00/0

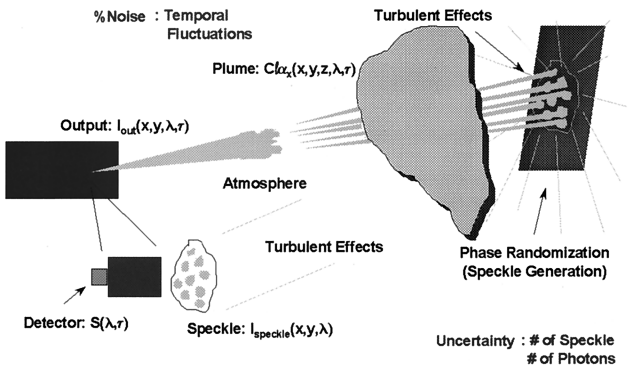

Fig. 1. Propagation scheme of lidar highlighting effects of the atmosphere and the target on the return signal.

front of the propagating beam introduced by spatial fluctuations in the index of refraction.[12–15] The three most dominant spatial effects are short-term beam spreading, beam wander, and scintillation. Short-term beam spreading causes the transverse optical profile to broaden spatially as a pulse propagates, becoming larger than a diffraction-limited pulse.[16] Beam wander is the motion of the beam centroid from pulse to pulse, which contributes to long-term beam spreading.[17] Finally, there is scintillation of the beam which is the temporal and spatial fluctuation in the laser irradiance.[18,19] All these variations can be predicted only statistically for given turbulence conditions, as the specific variations in the phase front will generally differ from one lidar pulse to another. The combination of these effects influences the contribution of the atmospheric component to the lidar return signal fluctuations.

The target surface also plays an important role in determining the nature of the return signal. A surface that is rough on the scale of the laser wavelength scatters the coherent laser pulse in all directions, producing a complex interference pattern.[20,21] This interference pattern is granular in appearance and is commonly referred to as a speckle pattern. The correlation area of these speckle is one parameter that is used to describe the pattern's statistical properties. Consider the case in which the receiver subtends a single speckle and an independent speckle pattern is observed in each measurement. In this case, the normalized standard deviation of intensity for a series of such measurements has a value of one (100% noise). This level of noise will exist even for larger return signal values. Similarly, if the receiver aperture subtends N_S speckle correlation areas, the standard deviation associated with a sequence of measurements of the energy in a speckle field scales roughly as $1/\sqrt{N_S}$.[20,22] Another example involves the completely static case in which there is no process that changes the speckle pattern from one pulse to the next. In this case, the standard deviation is zero (because the measurement does not change). However, the accuracy of such a measurement for a point detector is extremely low because the integrated intensity of the return signal is completely dependent on the point in the speckle field, bright or dark, that is being sampled. Ensemble averaging of independent speckle patterns will reduce the noise variance. The overall standard deviation for a collection of N_p return pulses, in which the receiver aperture integrates an average of N_S speckle per pulse, is $1/\sqrt{N_S N_p}$.

Previously we reported differences in measured noise levels for low- and high-turbulence conditions.[23,24] The lidar system used for these measurements was a finite-aperture system employing a scheme similar to the one shown in Fig. 1. Current lidar models do not generally account for the effect that variations in atmospheric turbulence will have on the noise and hence the detection limit of our system. In fact, estimation of noise in lidar systems often neglects the atmospheric turbulence component because the process is complex and has traditionally been dealt with only in a highly parameterized, statistical manner.[25] An analytical description of the interaction of these two processes that characterizes the electric field at the lidar receiver has been attempted.[26] The analytical approach gives predictions for point receivers that are not generally applicable to large-aperture lidar systems. Attempts to extrapolate these approaches to finite apertures are incomplete.[27] It is clear that another approach to this problem is needed.

A computer model to simulate the effects of atmospheric optical turbulence and reflective speckle on lidar performance is useful for studying different lidar situations. In this research, our goal is to ensure that our simulation will predict each of the separate effects of atmospheric optical turbulence and reflective speckle independently. In Section 2 we develop our beam propagation model. In Section 3 we compare the performance of our model with actual CO_2 lidar measurements of the separate effects of atmospheric turbulence and reflective speckle. We also compare the performance of our model with separate analytical predictions of atmospheric turbulence and reflective speckle. In addition, we present simulation results of the combined effects on a finite-aperture lidar system that are qualitatively consistent with previous experimental observations of increasing rms noise with increasing turbulence level. We summarize our findings in Section 4 and discuss our findings relative to previous research in this field.

2. Model

We are interested in the return signal of a lidar at wavelength λ_i obtained after a round trip through a plume containing a chemical species. The signal, integrated over the area of the receiver aperture, can be expressed as[10,28–30]

$$U_i = \frac{W_i}{\pi L^2} f(T_i, R_i, \ldots) Q_i \exp(-2C_a l \alpha_i), \qquad (1)$$

where W_i is the transmitted energy and L is the transmitter-to-hard-target propagation distance.

The exponential term in Eq. (1) denotes absorption by a chemical species of concentration C_a and absorption coefficient α_i within a uniform plume through which the beam propagates a distance l. We separated the absorption by the chemical species from the atmospheric transmission, contained in $f(T_i, R_i, \ldots)$, to reflect that the chemical plume is present over only a small part of the propagation distance. Q_i is a system-dependent constant for lidar returns at wavelength λ_i and includes the effect of varying the receiver area as well as other system parameters. In general, the variables on the right-hand side of Eq. (1) have a time dependence and can cause fluctuations in the return signal U_i.

The function $f(T_i, R_i, \ldots)$ expresses the round-trip transmission that includes the propagation effects of atmospheric absorption and atmospheric optical turbulence (indicated by T_i), target effects such as reflective speckle and albedo (denoted by R_i), as well as other effects. Other representations of the lidar equation have expressed the components of $f(T_i, R_i, \ldots)$ separately.[10,28,29] In general, however, these terms are interdependent and therefore we did not isolate them. A key factor in this interdependence, for example, is that both atmospheric optical turbulence and reflective speckle affect the phase of the propagating electric field. Atmospheric optical turbulence also alters the distribution of beam energy on the hard target, ultimately influencing the speckle correlation area.

Consider the special case in which only variations in $f(T_i, R_i, \ldots)$ contribute to the fluctuations in the return signal σ_{U_i}. There are a number of different sources of variations in $f(T_i, R_i, \ldots)$. These include changes in atmospheric absorption, fluctuations in the spatial distribution of energy on the target and at the receiver caused by atmospheric turbulence effects, variations in the intensity of the received reflective speckle, and hard-target albedo changes. In the model that follows, we consider only those contributions to the time dependence of $f(T_i, R_i, \ldots)$ caused by atmospheric optical turbulence and reflective speckle.

Our approach to modeling the effects of reflective speckle and atmospheric turbulence consists of applying a Huygens–Fresnel wave optics computer simulation, previously developed at the Naval Postgraduate School, to our lidar geometry.[31] This is an accepted approach for modeling the effects of atmospheric optical turbulence on the propagation of a laser beam to a target with no hard-target reflection.[32] Other numerical approaches that model Gaussian beam propagation have met with success as well.[33,34] Simulations of the double pass of an optical wave through a phase screen after reflection from a mirror have been done to examine enhanced backscatter.[35] A related speckle modeling approach, which neglected atmospheric turbulence effects, used Fresnel propagation to simulate the creation of a speckle pattern and determine the number of speckle integrated in a receiver aperture for different target geometries.[36] Another method for modeling speckle, which did not incorporate beam propagation, utilized a one-dimensional imaging approach to analyze the speckle intensity distribution and contrast as a function of surface roughness and the point spread of the imaging system.[37] An approach to the combined speckle–turbulence problem, which is conceptually similar to our turbulence propagation model, has provided some comparisons of probability density functions of received backscattered intensity with analytical approximations for point receivers.[38]

In our model, the phase front of the beam is distorted as it propagates to the target by a series of phase screens that simulate atmospheric turbulence effects. To simulate the diffuse hard-target production of reflective speckle, a random phase is added to the electric field phase term of the entire beam at the target. This distorted phase front then propagates through the same turbulent path.

In Appendix A, we discuss the approach of Davis[39] that uses the Fresnel–Kirchhoff theorem to approximate the electric field at an observation point in cylindrical coordinates as[40,41]

$$E(\hat{r}, z) = -\frac{i}{\lambda}\iint_A E(\hat{\rho}, z)\,\frac{\exp[ik(z^2 + |\hat{r} - \hat{\rho}|^2)^{1/2}]}{(z^2 + |\hat{r} - \hat{\rho}|^2)^{1/2}}\,\mathrm{d}A. \tag{2}$$

Propagation is in the z direction, $\hat{r}$ represents the position vector of the observation point in the x–y plane, and $\hat{\rho}$ is the position vector of the radiating point in the aperture plane. $E(\hat{\rho}, z)$ is the electric field originating in the transmitter aperture of surface area A. After assuming on-axis paraxial propagation along with the Fresnel approximation, we can write a propagation step symbolically, after some math, as

$$E(\hat{r}, z) \approx \mathrm{IFT}\{\exp(-i\pi\lambda z|\hat{f}|^2)\mathrm{FT}[E(\hat{\rho}, 0)]\}, \tag{3}$$

where FT is the two-dimensional Fourier transform and IFT is the two-dimensional inverse Fourier transform. This is an expression for the electric field at a propagation distance z in terms of the Fourier transform of the electric field at $z = 0$ with $\exp(-i\pi\lambda z|\hat{f}|^2)$ as the Fresnel propagator in frequency space $\hat{f}$.

The form of approximation (3) lends itself to numerical FT techniques and forms the basis of the wave optics simulation. We implemented this Huygens–Fresnel wave optics simulation using an $N \times N$ array of complex numbers to represent the electric field in a plane perpendicular to the propagation axis. The initial electric field, a Gaussian TEM_{00} spatial intensity and phase distribution with the characteristics of our experimental transmitter beam, is used as the input for the simulation. The simulation propagates this initial electric field by dividing the path from the lidar platform to the target into equal-sized steps and applying a phase screen to simulate turbulence at each step. As in approxima-

tion (3), the expression for the electric field after a step over a distance Δz is determined from

$$E(\hat{\rho}, \Delta z) = \mathrm{IFT}(\exp(-i\pi\lambda\Delta z|\hat{f}|^2)\mathrm{FT}\{E(\hat{\rho}, 0)\exp[i\theta(\hat{\rho})]\}), \tag{4}$$

where $E(\hat{\rho}, 0)$ is the electric field at the beginning of the step ($z = 0$). As before, FT is the discrete two-dimensional Fourier transform, $\exp(-i\pi\lambda\Delta z|\hat{f}|^2)$ is the Fresnel propagator in frequency space $\hat{f}$, λ is the lidar wavelength, and IFT is the discrete two-dimensional inverse Fourier transform. The phase screen $\theta(\hat{\rho})$ is given by[31,42]

$$\theta(\hat{\rho}) = 0.0984k_0\sqrt{C_n^2(z)\Delta z}\,(N\delta x)^{5/6} \times \mathrm{FT}[(\sqrt{n_x^2 + n_y^2})^{-11/6}\Theta_0(n_x, n_y)], \tag{5}$$

where $k_0 = 2\pi/\lambda$, $C_n^2(z)$ is the path-dependent index of refraction structure constant that parameterizes the level of turbulence,[13] Δz is the step propagation distance, N is the number of pixels along one dimension of the array, $\delta x = \sqrt{\lambda L/N}$ is the optimized pixel size for a transmitter-to-hard-target distance of L, n_x and n_y denote integer pixel coordinates within the two-dimensional array, $\Theta_0(n_x, n_y)$ represents an $N \times N$ array of complex unit-variance Gaussian random numbers, and FT again implies a two-dimensional discrete Fourier transform. The optimized pixel size $\delta x = \sqrt{\lambda L/N}$ is based on the work of Knepp[42] and Davis,[39] which takes into account the Nyquist criterion for sampling at an optimal spatial frequency. The argument of the FT operation is an array in the spatial frequency domain produced by one taking a Gaussian random number distribution and applying the $[(n_x^2 + n_y^2)^{1/2}]^{-11/6}$ factor to impose properties of the Kolmogorov spectrum, which describes the spatial frequency distribution of index of refraction fluctuations in the transverse plane.[32] As can be seen in Eq. (5), the strength of the turbulence phase screen depends on the level of turbulence, the length of the propagation step, and the wavelength. Figure 2 shows a typical phase screen.

The criteria for selecting the size of a propagation step Δz are twofold. The assumptions used to approximate a propagation step by use of approximation (3) dictate that the step be within the near field. Because our laser beam is approximated as a Gaussian TEM_{00} transverse mode, a step within the Rayleigh range is in the near field. The turbulence level also has an impact on the size of this step because the phase effects over this step must not be dominated by amplitude effects that arise from diffraction and interference as the distorted phase front propagates. Martin and Flatté[43] found that for the phase screen approach to be valid, the normalized point irradiance variance σ_I^2, defined below, for a propagation step must be less than 0.10 of the total normalized point irradiance variance for the entire propagation distance L:

$$\sigma_I^2(\Delta z) < 0.1\sigma_I^2(L). \tag{6}$$

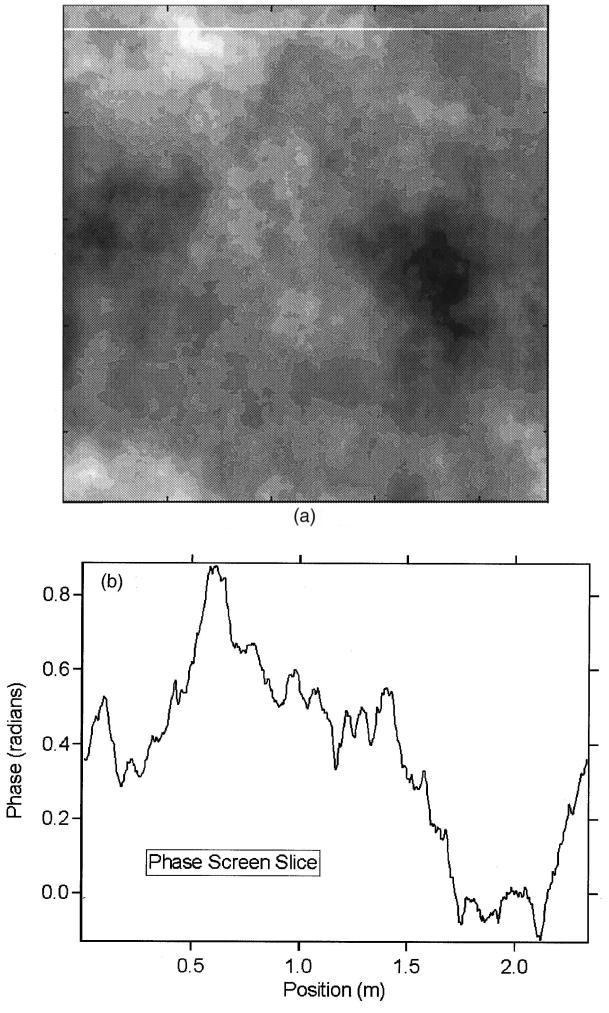

Fig. 2. (a) Phase screen for a 200-m step, turbulence level $C_n^2 = 10^{-14}\ \mathrm{m}^{-2/3}$, and wavelength 10.6 μm. Each pixel in the array is square and is 0.0046 m wide. Considering the phase for each of the 512×512 (262,144) pixels, the phase ranges from −1.0671 to 0.9490 rad. The mean phase is zero radians with a standard deviation of 0.3402 rad. (b) Slice of the phase screen indicated by the white line in (a).

They also found that this variance must be less than 0.1 for one step:

$$\sigma_{\bar{I}}^2(\Delta z) < 0.1. \tag{7}$$

For propagation of a spherical wave, assuming weak turbulence, the rms noise or scintillation at an on-axis point detector is[44]

$$\sigma_{\bar{I}} = [\exp(4\sigma_\chi^2) - 1]^{1/2}, \tag{8}$$

where $\sigma_I = \sigma_I/\bar{I}$ is the normalized standard deviation of irradiance. This is the square root of the normalized point irradiance variance mentioned above. The parameter σ_χ^2 is the spherical wave log-amplitude variance for a point detector. For a horizontal path of length L with uniform turbulence (i.e.,

constant C_n^2), the spherical-wave log-amplitude variance is[13]

$$\sigma_\chi^2 = 0.124 C_n^2 k_0^{7/6} L^{11/6}, \quad (9)$$

again with $k_0 = 2\pi/\lambda$.

At the target, the electric field phase is randomized to simulate reflective speckle with the expression

$$E(n_x, n_y)_{\text{reflected}} = E(n_x, n_y)_{\text{target}} \times \exp[i2\pi \text{ random}(n_x, n_y)], \quad (10)$$

where $E(n_x, n_y)_{\text{reflected}}$ is the electric field reflected from the target, (n_x, n_y) again denotes a pixel location within the transverse two-dimensional array, $E(n_x, n_y)_{\text{target}}$ is the complex electric field incident on the target after propagation through turbulence, and random(n_x, n_y) is a random number between 0 and 1 chosen from a uniform distribution. A uniform distribution is used because this is a good approximation for the phase produced by a surface that is rough compared to a wavelength of the coherent light on the target.[45] The reflected electric field then propagates back to the telescope and receiver with turbulence effects induced by use of the same phase screens as on the path out. The same phase screens are used because the atmosphere is considered frozen during the transit time of the lidar pulse. At the receiver, the electric field is used to determine the irradiance with the relation $I(\hat{\rho}, 2L) \propto E^*(\hat{\rho}, 2L) E(\hat{\rho}, 2L)$, where $E^*(\hat{\rho}, 2L)$ indicates the complex conjugate of the electric field at the receiver after propagation through a round-trip distance $2L$. The irradiance is integrated over the particular receiver area to determine the return signal. This return signal is analyzed over a number of atmospheric turbulence and target phase realizations. These different realizations produce changes in the received speckle pattern and vary the return signal from one pulse to the next.

In modeling the round-trip propagation, there are a number of transverse scales that one must consider. The simulation must be able to accommodate the larger scales without allowing energy to be artificially reflected back into the grid. The initial output beam width as well as the diffraction-limited beam width at the target must be small enough in comparison to the overall simulation grid to minimize any unphysical reflection. Turbulence-induced beam spreading must also be contained in the simulation grid. In general, a beam diameter less than half of the simulation grid width at any point along the propagation path is sufficient to mitigate the artificial reflection of beam energy. For the reflection of energy from the rough target, the paraxial assumption, on which the numerical model is based, reduces the amount of energy that propagates to the edges of the simulation grid.

The numerical simulation must also be capable of sampling the transverse electric field at a spatial frequency large enough to provide satisfactory modeling and assessment of the overall propagation effects. To determine the speckle correlation diameter, for example, there must be an adequate number of pixels that make up each speckle. For small speckle or coarse grids, the sampling would be unsatisfactory. We never approach this regime for the lidar geometries modeled in this research. For example, the smallest number of pixels per speckle correlation area in this research is ~16. The turbulence-induced transverse coherence length of the electric field and the characteristic size of scintillation should also never approach the pixel size. Large values of path-integrated turbulence effects in the strong turbulence regime would prove troublesome.

3. Simulation Results and Discussion

A. Atmospheric Turbulence Effects

Although in general the ability of the Huygens–Fresnel approach to simulate the effects of atmospheric optical turbulence is well established,[31,32,43,46] this approach has certain limitations that may limit its usefulness for specific systems. One possible limitation is that the Fourier representation of the phase screens underestimates the large-amplitude, low-frequency components of the Kolmogorov spectrum, which characterizes atmospheric turbulence. Consequently, this may lead to less beam wander than would be measured experimentally. The Fresnel approximation, inherent to the method, constrains the length of the propagation steps as mentioned above. If an excessive number of propagation steps are used, it could lead to a disproportionate amount of computation time. Therefore one goal is to keep the number of steps as low as possible. In addition, as mentioned above, the maximum size of the beam on the target must be limited so that one may avoid spillover of energy off the grid. We also realize that small spatial variations are not adequately modeled by this simulation because of aliasing effects inherent in FT techniques. It is therefore necessary and instructive to verify the application of this method to specific propagation problems. Here we verify the validity of the simulation for our geometry by comparing results from it with analytical models and experimental results. Figure 3(a) is an example of an irradiance pattern from the simulation for a case of zero turbulence ($C_n^2 = 0$). In Fig. 3(b) we used a higher level of turbulence ($C_n^2 = 10^{-14}\ \text{m}^{-2/3}$) that is at approximately the midrange of the values that we measured during summer in the Nevada desert. The effect of turbulence on the beam is readily apparent in the image of Fig. 3(b).

1. *Long-Term Beam Spreading*

One effect of turbulence that we observed in our lidar system is that of long-term beam spreading, which is a combination of short-term beam spreading and centroid motion over many pulses. We begin with the analytical prediction of such spreading. Ignoring platform motion, we can express the effective diameter ($1/e^2$ intensity) of a laser beam propagating

through a turbulent atmosphere as the combination of two independent effects by[47,23]

$$D^2 = 8(\alpha_d{}^2 + \alpha_t{}^2), \tag{11}$$

where $\alpha_d{}^2$ and $\alpha_t{}^2$ refer to the contributions that are due to diffraction and atmospheric turbulence, respectively. The long-term turbulence contribution is

$$\alpha_t = \frac{\lambda L}{\pi \rho_0}, \tag{12}$$

where λ is the laser wavelength and L is the propagation distance. The transverse coherence length ρ_0 is the distance transverse to the propagation direction where the average electric field correlation falls to $1/e$ of its fully correlated value.[48]

The transverse coherence length can be expressed for three cases. For the plane-wave limit it is given by[49]

$$\rho_{0-\text{plane}} = \left[1.46 k_0{}^2 \int_0^L C_n{}^2(z)\mathrm{d}z\right]^{-3/5}, \tag{13}$$

and for the spherical-wave limit,[49]

$$\rho_{0-\text{spherical}} = \left[1.46 k_0{}^2 \int_0^L C_n{}^2(z)\left(\frac{z}{L}\right)^{5/3}\mathrm{d}z\right]^{-3/5}, \tag{14}$$

where $k_0 = 2\pi/\lambda$ and $C_n{}^2(z)$ is the index of refraction structure constant denoting the strength of atmospheric turbulence. For a beam wave or a Gaussian beam, the expression for transverse coherence length is[13]

$$\rho_{0-\text{Gaussian}} = \rho_{0-\text{plane}}\left\{\frac{\left(1-\frac{L}{f_l}\right)^2 + \frac{4L^2}{k_0{}^2 D_x{}^4}\left[1+\frac{1}{3}\left(\frac{D_x}{\rho_{0-\text{plane}}}\right)^2\right]}{1-\frac{13}{3}\left(\frac{L}{f_l}\right)+\frac{11}{3}\left(\frac{L}{f_l}\right)^2+\frac{4L^2}{3k_0{}^2 D_x{}^4}\left[1+\frac{1}{4}\left(\frac{D_x}{\rho_{0-\text{plane}}}\right)^2\right]}\right\}^{1/2}, \tag{15}$$

where D_x is the transmitted beam diameter and f_l is the radius of curvature. The value of $\rho_{0-\text{Gaussian}}$ will fall between the extremes of $\rho_{0-\text{plane}}$ and $\rho_{0-\text{spherical}}$.

Experimentally, we quantified the transverse laser beam profile in the target region by scanning the beam over a narrow vertical pole in our target area and measuring the return signal at each position in the scan.[23] The beam scan was performed slowly over a large number of pulses to quantify the long-term spreading effect. We concurrently measured the atmospheric turbulence through use of a combination of scintillometers and point temperature probes.[23,50] The propagation path was horizontal over flat, featureless desert terrain with a range of 3300 m. The turbulence along this path was assumed to be uniform.

In Fig. 4 we present the long-term beam-spreading effects (which include the effects of short-term beam spreading and centroid motion) observed in several experimental profiles. They are compared with those observed in the simulation and predicted by analytical models for beam propagation in turbulence.[23] We calculated the analytical values for plane-wave, spherical-wave, and beam-wave cases assuming uniform turbulence over a horizontal propagation path and using Eqs. (11) and (12) taking system beam parameters into account.[12,14] Transverse coherence lengths for plane wave, spherical wave and Gaussian beams were calculated with Eqs. (13)–(15), respectively.

For the simulation, a total of 100 independent turbulence realizations were summed to generate the long-term beam-spreading effect. Columns of pixels in the resulting pattern were then summed to generate a one-dimensional intensity pattern, mimicking the scanning of a beam across a pole. A least-squares curve fit to this profile was used to determine the Gaussian beam parameter for the simulation. The simulation used five propagation steps on a 512×512 array and was repeated for each turbulence level. The lidar beam was modeled to closely match the experimental beam with a beam diameter of 0.207 m and an initial radius of curvature f_l of 843 m. This is indicative of a beam that is initially converging to a focus in front of the transmitter output and diverges beyond that point. There is good agreement between the simulation and the analytical theory that uses the spherical-wave transverse coherence length in Eq. (12). This conforms with previous research in Gaussian beam spreading.[13,14,16,51] There is also agreement in the trend with increasing atmospheric optical turbulence evident in the experimental data.

2. *Scintillation*

A second turbulence effect is scintillation, the temporal and spatial fluctuation of intensity. Figure 5 shows the comparison between simulation and the analytical expression of Eq. (8). The value of $\sigma_\chi{}^2$ for this beam-wave case, following Miller *et al.*,[52] is given by

$$\sigma_\chi{}^2 = 0.0675 C_n{}^2 k_0{}^{7/6} L^{11/6}, \tag{16}$$

where the constant 0.0675 is based on an output beam that is 0.075 m in diameter with a radius of curvature of 601 m (initially converging) for the

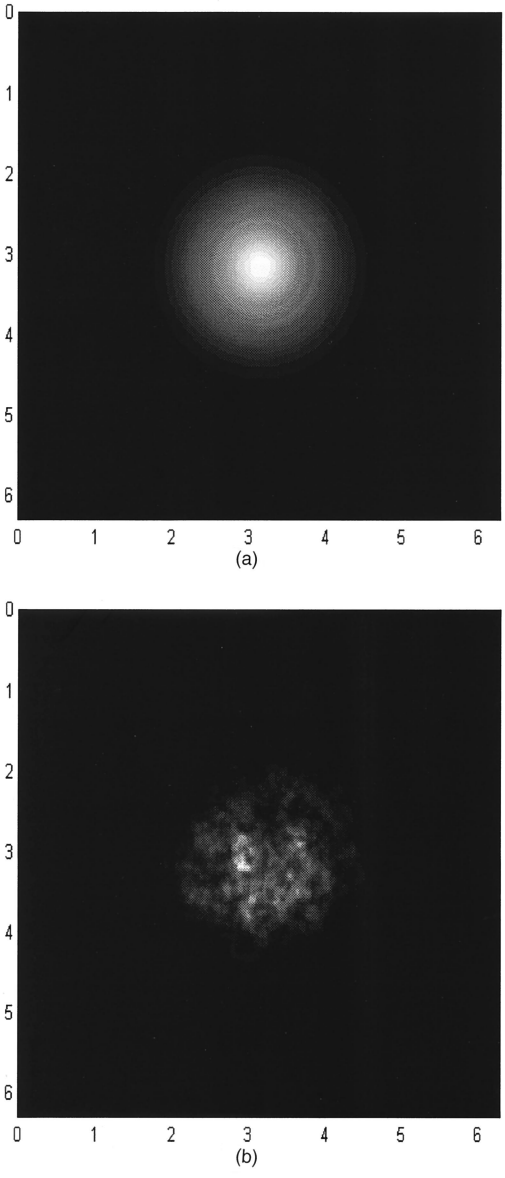

Fig. 3. Computer images of a 10.6-μm Gaussian beam intensity on target. Propagation distance is 7300 m and the diffraction-limited beam divergence is 0.290 mrad. Axis values are in meters. The simulation used 10 propagation steps of 730 m each with a 512 × 512 array: (a) with zero turbulence and (b) a uniform turbulence level of $C_n^2 = 10^{-14}$ m$^{-2/3}$. The modeled beam path is horizontal and ~3 m above the ground.

~200-μrad divergence case. The propagation geometry involves a one-way 2000-m trip to the target where the scintillation values are obtained. The simulation consisted of five propagation steps and a 512 × 512 array. For each of the 100 pulses simulated, the turbulence was modeled as uncorrelated from pulse to pulse. The simulated detector area is that of one pixel (0.0064 m × 0.0064 m) and is as close to a point detector as the simulation allows. There is good agreement in the weak turbulence regime. The simulated values assume uncorrelated rms noise, and the error bars reflect the fact that 100 pulses were modeled.

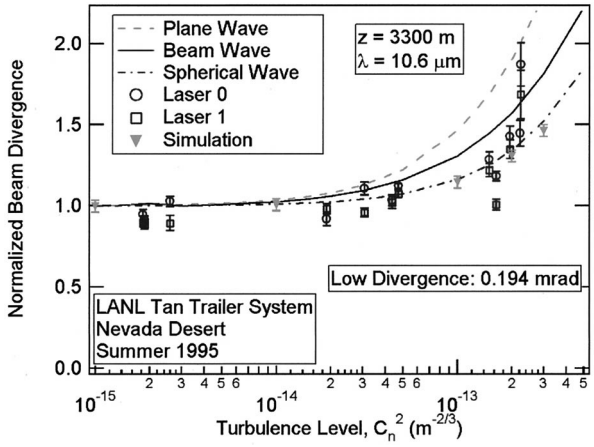

Fig. 4. Comparison of experimental and simulation data of the beam-profiling experiment with analytical theory. Beam profile measurements of CO_2 lidar were for a propagation path of 3300 m. Measurements were taken by scanning the beam across a pole and determining the best-fit Gaussian profile. In the simulation, a total of 100 pulses were summed to obtain the long-term beam-spreading effect. Columns of pixels in the resulting pattern were then summed to mimic the effect of scanning a pole, resulting in a one-dimensional profile. A best-fit Gaussian to this resulting profile was determined to obtain the beam size. Laser 0 and laser 1 are the designations used for the two lasers in our system. The simulation used five propagation steps and a 512 × 512 array. The beam divergence was normalized by its diffraction-limited value. LANL, Los Alamos National Laboratory.

Figure 6 shows a comparison of the off-axis behavior of scintillation as observed in the simulation with the analytical theory predicted by Miller *et al.*[52] In both cases the rms noise or $\sigma_{\bar{I}}$ increases with radial distance from the beam center. The simulation values are indicative of one-pixel detectors (0.0046 m × 0.0046 m). The simulated output lidar beam for this case had a diameter of 0.075 m and a radius of curvature of 139 m (initially converging). The simulation grid was 512 × 512 and utilized 20 phase screens

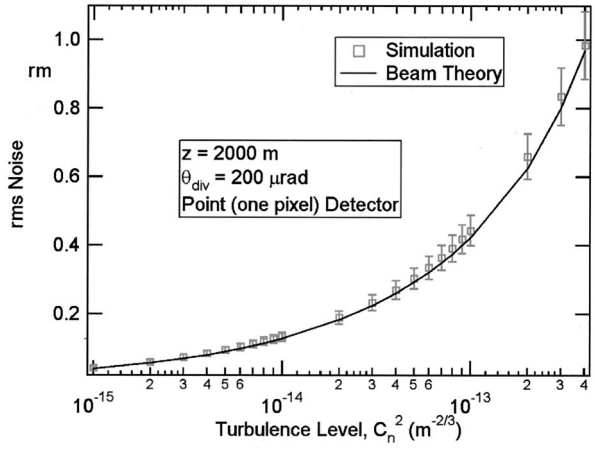

Fig. 5. Scintillation of a 10.6-μm lidar beam for a point (one pixel) detector after a 2-km propagation through different levels of optical turbulence. The error bars are estimated from the 100 samples in each simulation.

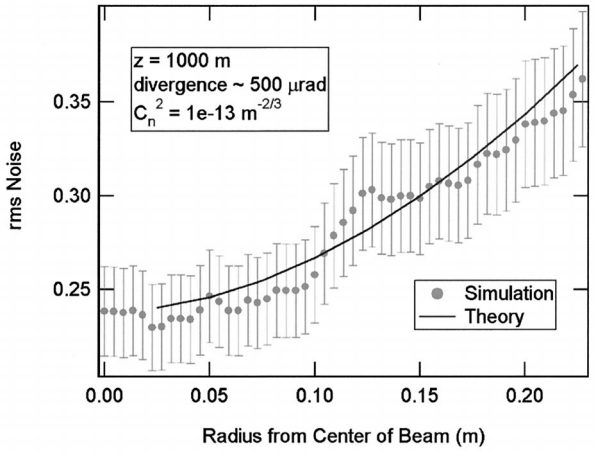

Fig. 6. Off-axis variation of scintillation as a function of radius from the center of a 10.6-μm Gaussian beam. The beam had an angular divergence of 500 μrad and propagated 1 km through a turbulence level of $C_n^2 = 10^{-13}$ $m^{-2/3}$. The error bars are estimated from the 100 samples in the simulation.

that modeled 100 pulses. Again we see good agreement between our simulation and analytical theory.

3. *Transverse Coherence Length*

Another turbulence effect is the decrease in spatial coherence transverse to the propagation direction which was mentioned above.

Figure 7 is a plot of transverse coherence length ρ_0 obtained from the simulation compared with plane-wave, spherical-wave, and beam-wave analytical theory of Eqs. (13)–(15). The simulated values were calculated from[39]

$$\mathrm{MTF}_{\mathrm{atmosphere}} = \exp\left[-3.44\left(\frac{\hat{r}}{r_0}\right)^{5/3}\right], \qquad (17)$$

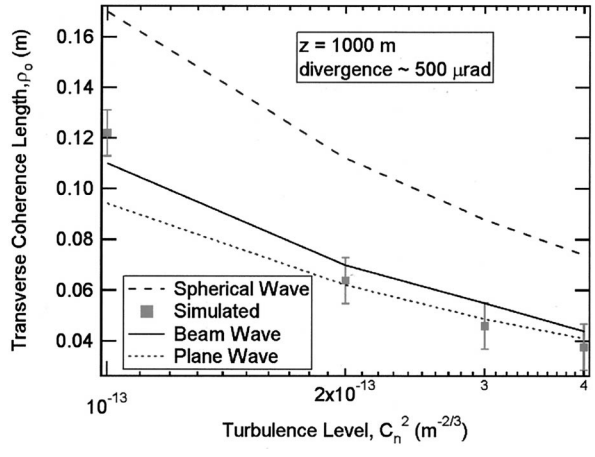

Fig. 7. Transverse coherence length of a 10.6-μm Gaussian beam after a propagation of 1 km for different amounts of optical turbulence. The beam had a 500-μrad angular divergence. Simulation values were obtained from the long-term atmospheric modulation transfer function and are compared with the analytical theory for plane wave, spherical wave, and Gaussian beam. The error bars are estimated from the resolution of the simulation grid.

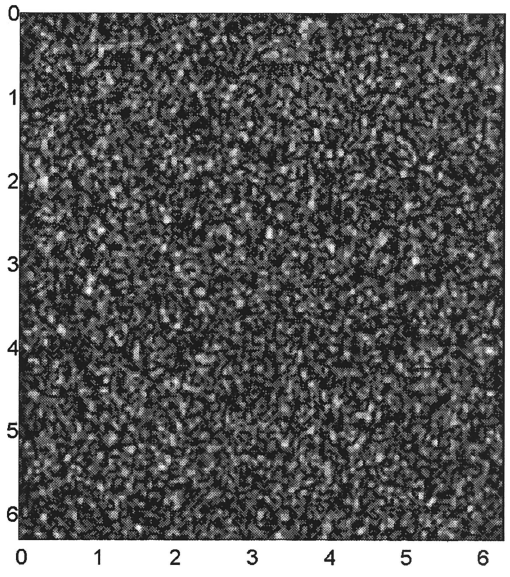

Fig. 8. Simulated reflective speckle pattern at the receiver for the case shown in Fig. 3(a) except that the beam divergence has been changed to 0.160 mrad. This smaller beam divergence provides for a better illustration with a larger speckle correlation diameter.

where $\mathrm{MTF}_{\mathrm{atmosphere}}$ is the long-exposure atmospheric modulation transfer function, $r_0 = 2.1\rho_0$ is the Fried parameter, and $\hat{r}$ is the radial distance from the center of the $\mathrm{MTF}_{\mathrm{atmosphere}}$. The half-width at half-maximum (HWHM) of the $\mathrm{MTF}_{\mathrm{atmosphere}}$ provided us a means of determining $\rho_{0-\mathrm{Gaussian}}$ from the simulation and was described by Davis.[39] Simulation values of $\rho_{0-\mathrm{Gaussian}}$ exhibit the expected decrease in size with increasing turbulence and lie between the plane-wave and spherical-wave predictions. The simulated lidar beam had an output diameter of 0.075 m and a radius of curvature of 139 m (initially converging). A total of 100 pulses were numerically simulated on a 512 × 512 grid with 20 phase screens.

B. Reflective Speckle Effects

Our next step in determining the validity of this type of simulation for predicting the effects of atmospheric turbulence and reflective speckle is to establish the validity of the model in simulating reflective speckle alone. To accomplish this, we conducted a number of simulations for zero-turbulence conditions to compare with results from established theory describing effects of speckle. Figure 8 shows a typical speckle pattern at the receiver from our simulation for a zero-turbulence case with reflective speckle.

1. *Speckle Correlation Diameter*

One statistical property of a speckle pattern is the average speckle diameter. From the derivation of Goodman[20] and MacKerrow and Schmitt,[53] the speckle correlation diameter can be estimated from the width of the spatial autocorrelation function of

the intensity distribution in the plane of the receiver given by

$$R_I(x_1, y_1; x_2, y_2) = \langle I(x_1, y_1) I^*(x_2, y_2) \rangle, \qquad (18)$$

where the angled brackets indicate an ensemble average over statistically independent speckle patterns. The derivation uses the Fresnel approximation with the Huygens–Fresnel principle, which is completely analogous to the assumptions used in our model and assumes fine-surface variations that are unresolvable by the lidar telescope. With these assumptions, after some manipulation, the autocorrelation for the intensity of a TEM_{00} Gaussian beam becomes[20,53]

$$R_I(\Delta x, \Delta y) = \langle I \rangle^2 \left(1 + \exp\left\{ \frac{-\pi^2 {w_T}^2}{\lambda^2 z^2} [(\Delta x)^2 + (\Delta y)^2] \right\} \right), \qquad (19)$$

where $\Delta x \equiv (x_1 - x_2)$ and $\Delta y \equiv (y_1 - y_2)$ are separations within the speckle pattern, w_T is the laser spot size (radius) on the target, z is the distance from the TEM_{00} Gaussian illumination or target plane to the speckle pattern plane, $\langle I \rangle$ is the mean intensity, and λ is the lidar wavelength. Defining the correlation diameter d_c as the point where the diameter of the complex coherence portion (the exponential term) of the autocorrelation function, Eq. (19), has dropped to $1/e$ of its peak value, we obtain[53]

$$d_c = \frac{2\lambda L}{\pi w_T}, \qquad (20)$$

where λ is the wavelength of the lidar pulse, $z = L$ is the propagation distance from the target to the telescope, and w_T is the beam spot size (radius) on the target.

We determine the speckle correlation diameters in the simulation by calculating the square of the complex coherence factor, the exponential term of Eq. (19). In image processing terms, this is simply the normalized autocovariance and can be calculated from the intensity of a single-shot speckle pattern with fast FT techniques.[54] This formulation provides a speckle correlation diameter equivalent to the definition of the speckle correlation diameter given in Eq. (20). The normalized autocovariance is defined as[45]

$$C_{I_N} = \frac{\langle (I_1 - \langle I \rangle)(I_2 - \langle I \rangle) \rangle}{{\sigma_I}^2}. \qquad (21)$$

I_1 and I_2 denote the intensities at two different points, ${\sigma_I}^2$ represents the variance of the intensity over the points in the speckle pattern, and the angled brackets represent an ensemble average over the speckle pattern. We estimate the correlation diameter from the point where the normalized autocovariance function is $1/e$ of its peak value. Figure 9 is a comparison of the correlation diameters produced by the simulation for a number of different beam diameters at the target for zero turbulence with that predicted by Eq. (20). There is excellent agreement between the simulation coherence diameters and those expected from theory.

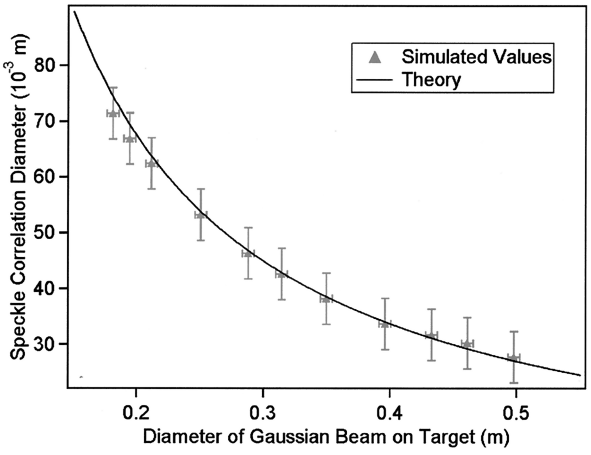

Fig. 9. Comparison of simulated speckle correlation diameter in zero turbulence with that predicted by theory as a function of beam diameter on target. A single-pulse simulation was used with five propagation steps on a 512×512 array. The $1/e$ value of the normalized autocovariance rendered the speckle correlation diameter. The simulated value errors bars represent one pixel width which is the resolution of the simulation. The analytical values are given by Eq. (20). Propagation range is 1000 m and the lidar wavelength is 10.6 μm.

2. Approximate Gamma Distribution

Although in principle the exact probability distribution function (pdf) for reflective speckle can be calculated with the Karhunen–Loeve expansion, to our knowledge the exact probability distribution function for a Gaussian TEM_{00} beam on target and a circular receiver has not been solved.[53] The probability density of return signal intensities are usually estimated by use of the approximate Gamma distribution developed by Goodman.[20,45] The result of Goodman's derivation is the approximate Gamma distribution, which is the pdf for the integrated intensity of a speckle pattern I_0 as[20]

$$p_{I_0}(I_0) \cong \begin{cases} \dfrac{1}{\Gamma(M)} \left(\dfrac{M}{\langle I \rangle} \right)^M {I_0}^{M-1} \exp\left(-M \dfrac{I_0}{\langle I \rangle} \right), & \text{if } I_0 > 0 \\ 0, & \text{otherwise} \end{cases} \qquad (22)$$

The factor M is usually interpreted as the number of speckle inside the receiver aperture for an average pulse, $\langle I \rangle$ is the mean value for the integrated intensity of the entire speckle pattern, and Γ is the gamma function. Examples of this distribution for different values of M are shown in Fig. 10. For a point detector, $M = 1$, and relation (22) simplifies to a negative exponential. If the receiver aperture area is smaller than the speckle correlation area, the value of M is unity. In such a case, the intensity measured at the aperture will be influenced by a single speckle even if

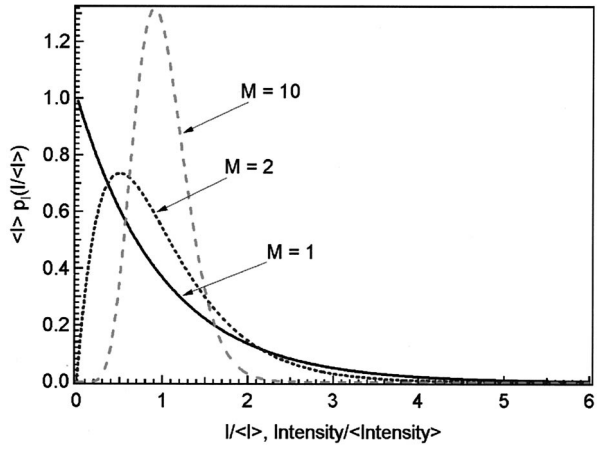

Fig. 10. Probability density function for measuring a speckled lidar return of intensity I, relation (22). M is approximately the number of speckle integrated by the receiver aperture on an average pulse. For $M > 10$ this function approaches a Gaussian pdf.

only a small fraction of the speckle is sampled. Values of $M < 1$ therefore have no physical meaning.

Goodman also defined a relationship that compares M with a signal-to-noise ratio.[21] His definition is

$$\left(\frac{\text{signal}}{\text{noise}}\right)_{\text{rms}} \equiv \frac{\langle I_0\rangle}{\sigma_{I_0}} = (M_{\text{exact}})^{1/2}, \tag{23}$$

where $\langle I_0\rangle$ is equal to the true mean of the speckle pattern and σ_{I_0} is the square root of the variance of integrated intensity. An approximate relationship is

$$\left(\frac{\text{signal}}{\text{noise}}\right)_{\text{rms}} \cong M^{1/2}, \tag{24}$$

which compares the value of M from relation (22) with calculated quantities from the intensity pattern generated by the simulation.

For a given lidar beam and receiver geometry, it is possible to calculate the value of M_{exact} based on the speckle area and the receiver area.[20,53] With a Gaussian TEM_{00} beam at the target and a circular receiver aperture, the geometrically calculated M_{exact}, $M_{\text{circ-Gauss}}$ is

$$M_{\text{circ-Gauss}} = \frac{\pi}{16}\left\{\int_0^1 dy[y\cos^{-1}(y) - y^2\sqrt{1-y^2}] \times \exp\left[-4\left(\frac{S_M}{S_C}\right)y^2\right]\right\}^{-1}, \tag{25}$$

where S_M is the receiver area and S_C is the speckle correlation area given by

$$S_C = \pi\left(\frac{d_C}{2}\right)^2 = \frac{\lambda^2 z^2}{\pi {w_T}^2}. \tag{26}$$

We can then compare the M found from the Gamma distribution fits in our simulation to the geometrically calculated $M_{\text{circ-Gauss}}$.

To compare our simulation to the theory outlined above, we simulated 1000 speckle pattern realizations for a number of different beam sizes on target. We then calculated the measured intensities for a number of circular receiver apertures of varying radii.

We fit the simulation intensity data to the approximate Gamma distribution of relation (22) to determine if the simulation produced the expected form of the pdf. When performing histograms of intensity values, the bin size is important when one is determining the pdf. The curve fits included our varying the bin sizes for histogramming intensity data from the simulation. We sampled the bin sizes such that the number of bins used varied from ~20 to ~200. We used the χ^2 distribution to test the suitability of our curve fits. The definition of χ^2 is[55]

$$\chi^2 = \sum_{j=1}^{\text{nbin}} \frac{[h(x_j) - N_{\text{tot}}P(x_j)]^2}{\sigma_j(h)^2}. \tag{27}$$

Here $P(x_j)$ is the value of the pdf at a particular bin location and N_{tot} is the total number of measurements. The product $N_{\text{tot}}P(x_j)$ is then the predicted number of measurements of intensity for a certain bin location and is equivalent to the Gamma distribution function given by relation (22). The value $h(x_j)$ is the actual number of measured intensities in each bin and nbin is the total number of bins. The standard deviation of the mean $\sigma_j(h)$ acts as a weighting function and is estimated from the simulation results by use of Poisson statistics with $\sigma_j(h) \propto \sqrt{N_{\text{bin}}}$ where N_{bin} is the number of counts per bin.[55] The reduced value of χ^2 is

$${\chi_\nu}^2 = \frac{\chi^2}{\nu_f}, \tag{28}$$

where $\nu_f = \text{nbin} - n_c$ and n_c are the number of constraints. The histogrammed simulation results and the Gamma distribution were normalized to calculate ${\chi_\nu}^2$. The probability of observing values of ${\chi_\nu}^2$ equal to or greater than our calculated value are distributed according to the χ^2 distribution. Fits that met the criteria of being near the center of the χ^2 distribution (0.50 ± 0.10) were used as acceptable curve fits resulting in simulated M values or M_{fit}. Several representative plots resulting from this method are shown in Fig. 11. The error bars of the histogrammed simulation results are based on the estimated value of $\sigma_j(h)$. The simulation comparison with theory shown here looks similar to previous research by MacKerrow and Schmitt[53] comparing their experiments with theory. Their experiments were conducted over a short path (115 m) in which the effects of atmospheric optical turbulence were small. We found that the simulation produced intensities that have the appropriate pdf's. The simulation therefore produced intensity distributions close to those that we would expect from both theory and experiment. Table 1 shows some examples of the parameters described above.

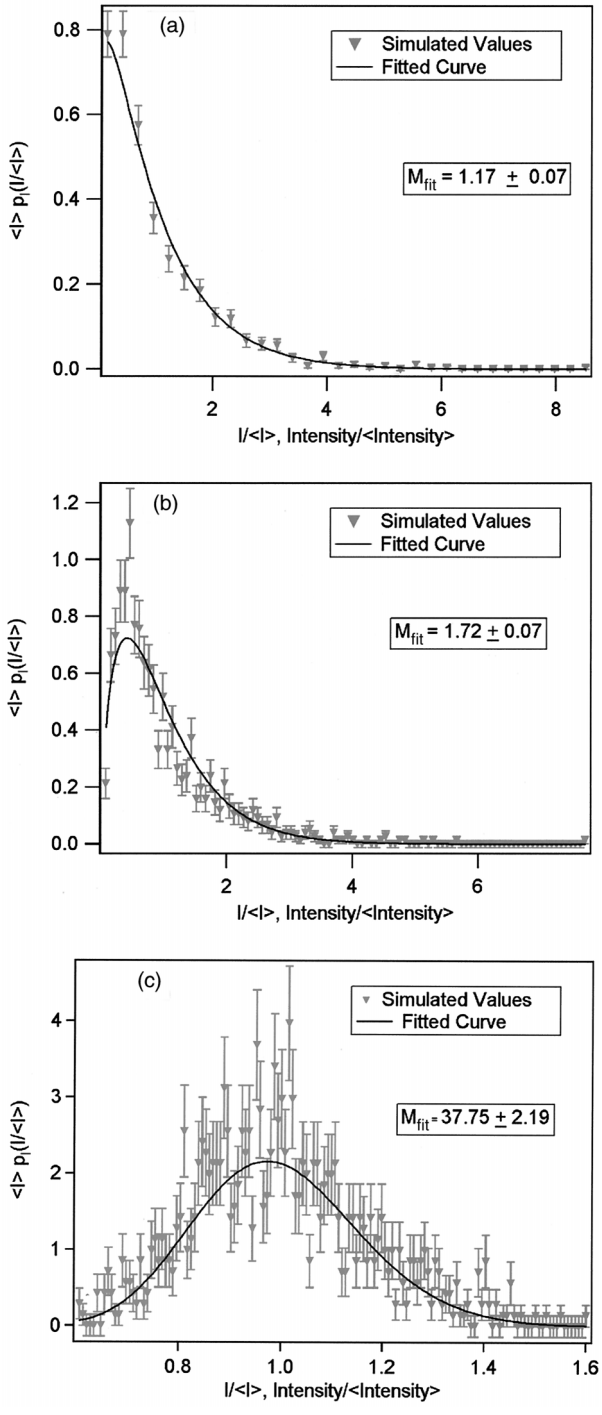

Fig. 11. (a) Simulated pdf for a receiver of radius ~1.4 cm with independent speckle realizations and zero turbulence ($C_n^2 = 0$). The diffraction-limited diameter of the beam on target ~0.20 m and $z = 1000$ m. The inverted triangles represent the distribution of simulated received intensity for 1000 pulses. The solid curve represents the best-fit Gamma distribution. This figure compares favorably with the $M = 1$ curve in Fig. 10. The simulation used five propagation steps on a 512×512 array. (b) Same simulation parameters as (a) except the receiver radius is ~2.3 cm. Note the similarity with the $M = 2$ curve in Fig. 10. (c) Same simulation parameters as (a) and (b) except the receiver radius is ~18.2 cm. The transition to a more Gaussian shape is apparent as with the $M = 10$ curve in Fig. 10.

Table 1. Sample M_{fit} Parameters for Different Receiver Aperture Sizes

Receiver Radius (m)	M_{fit}	χ_ν^2	χ^2 Distribution Value
0.0137	1.17 ± 0.07	0.984	0.49
0.0228	1.72 ± 0.07	0.968	0.57
0.0455	3.50 ± 0.18	1.002	0.46
0.0683	6.27 ± 0.29	0.977	0.52
0.0910	10.16 ± 0.45	0.908	0.58
0.1138	17.02 ± 0.91	1.005	0.47
0.1820	33.40 ± 1.69	1.013	0.44

We also compared our M_{fit} values with those calculated using Eq. (25) to numerically calculate $M_{circ\text{-}Gauss}$ values from the lidar geometry. In Fig. 12 the simulated M_{fit} values and S_M/S_C ratios are compared and show agreement to within ~10% of the $M_{circ\text{-}Gauss}$ values. This agreement is additional verification of the simulation regarding speckle for the particular geometry and receiver sizes of our system.

Another comparison involved our using M_{fit} and the measured signal-to-noise ratio from the simulation. Figure 13 shows agreement to within ~5% between the signal-to-noise ratio values obtained from theory and simulation when plotted versus the analytical M_{exact} and simulated M_{fit} values, respectively. Assuming linearly polarized light, we calculated the M_{exact} value through Eq. (23)[20]:

$$M_{exact} = \left(\frac{\text{signal}}{\text{noise}}\right)^2_{rms}, \tag{29}$$

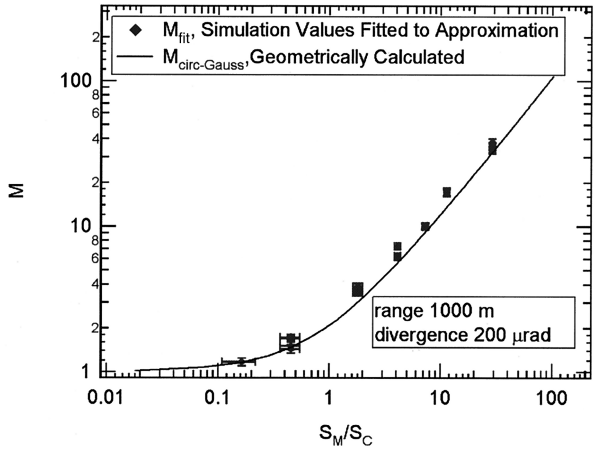

Fig. 12. Comparison of fitted values of M, M_{fit} versus ratio of the aperture area to the estimated correlation area from simulation and theory. The theoretical plots of M, $M_{circ\text{-}Gauss}$ are those predicted for Gaussian target illumination with a circular receiver aperture. S_M is the area of the receiver aperture and S_C is the average area of a speckle. We simulated 1000 pulses for a transmitter to a target distance of 1000 m. Five propagation steps on a 512×512 array were used. The beam diameter on target ~0.20 m. Curve fits were performed to determine the simulated M factor M_{fit}. The data points represent receiver apertures of different radii.

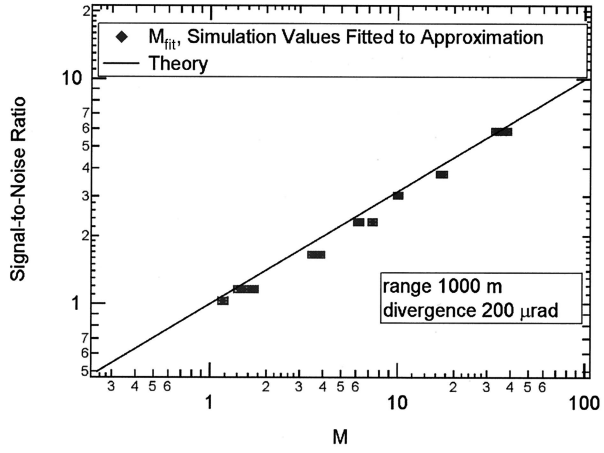

Fig. 13. Comparison of signal-to-noise ratio versus fitted M values, M_{fit}, from simulation and theory for the same data as shown in Fig. 12.

where $(\text{signal/noise})_{\text{rms}}$ is the signal-to-noise ratio of the simulated intensities I_0 measured by the receiver aperture. It should be emphasized that the value of M_{fit} that was determined from the curve fits to the Gamma distribution of relation (22) was not exact but the result of an approximation. Therefore, although the agreement in Fig. 12 is good, we do not expect a perfect comparison. Equation (23) is an exact relationship defined by Goodman[20] whereas relation (24) is an approximation based on the approximate Gamma distribution given in relation (22). Our results for comparison with theory of the simulated M_{fit} values shown in Figs. 11–13 show agreement with both theory and experiment.[53] This provides further verification that the M values of the fitted intensity distributions are appropriate when compared with the signal-to-noise ratio obtained from the simulation.

C. Combined Effects

The simulation provides a means of our examining the combined effects of atmospheric optical turbulence and reflective speckle for a finite-aperture lidar system. The results of combined effects of simulations for our lidar system are shown in Fig. 14. For the case shown in Fig. 14(a), the simulated lidar beam had an output radius of curvature of 139 m (initially converging). For the case shown in Fig. 14(b), the output radius of curvature was 601 m (initially converging). In both cases, a total of 100 pulses were numerically simulated on a 512×512 grid with five phase screens and an output lidar beam that was 0.075 m in diameter. The modeled lidar receiver is annular with an inner diameter of 0.118 m and an outer diameter of 0.0305 m. Note that there is a definite increase in rms noise for the larger values of C_n^2. These results indicate that atmospheric optical turbulence is an additional noise source for a finite-aperture lidar. This increase in rms noise qualitatively agrees with earlier observations.[23,24]

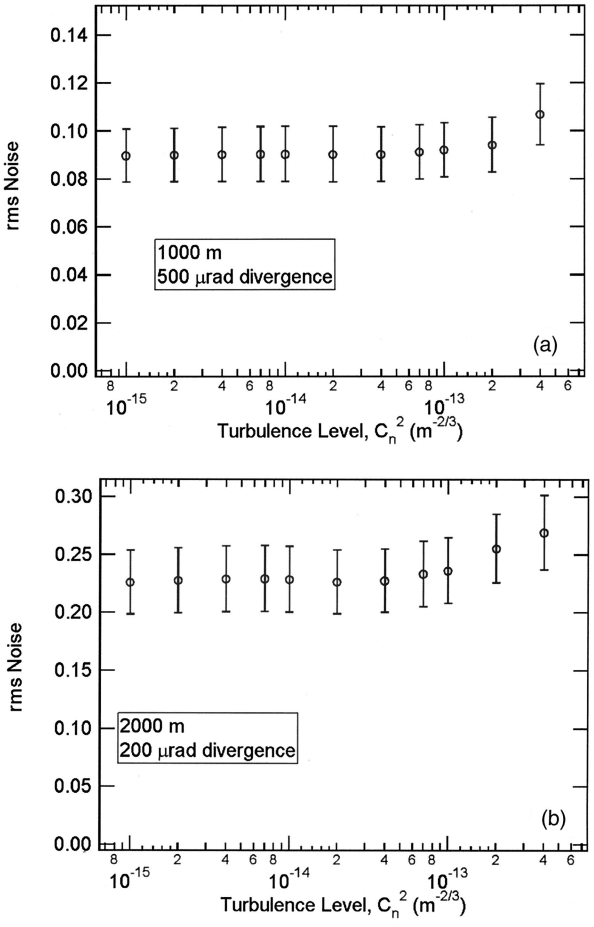

Fig. 14. (a) Shown are rms intensity fluctuations for a 0.075-m diameter, 10.6-μm Gaussian lidar beam scattered from a diffuse target for two-way propagation along a 1-km propagation path for different amounts of optical turbulence. The beam had a 500-μrad divergence. The error bars are estimated from the 100 samples in each simulation. (b) Same as (a) except the propagation path is 2 km and the angular divergence is 200 μrad.

4. Conclusions

We have used a Huygens–Fresnel wave optics computer simulation to model the effects of atmospheric turbulence and reflective speckle. In this initial research, we have addressed the ability of our code to simulate these effects separately. Our approach has been to compare results for each of these phenomena with a combination of analytical and experimental results. The atmospheric optical turbulence effects produced by our simulation for our lidar geometry agree well with experimental results and analytical predictions. The simulation for long-term turbulent beam spreading showed good agreement with both experimental data and analytical predictions. Simulation values for point detector scintillation that is due to turbulence, both on and off axis, also showed good agreement with theory. These results indicate that our simulation accurately predicts the effects of atmospheric turbulence for our lidar geometry.

Our investigation of the reflective speckle effects also showed good agreement with analytical and ex-

perimental results. The simulated speckle correlation diameters were in excellent agreement with those predicted by theory. The intensity distributions predicted by our simulation agreed with those observed in experiment and expected from theory and resulted in appropriate simulation fitted M values. Comparison of simulated fitted M values with those predicted through the geometry of the relative speckle correlation area and receiver area resulted in agreement to within ~10%. Comparison of the simulated signal-to-noise ratio versus the simulated fitted M values compared to within ~5% of theory. The results indicate that our simulation is valid for modeling the separate effects of atmospheric optical turbulence and reflective speckle.

Although each of these two separate phenomena is now characterized in our simulation, the interdependence of atmospheric optical turbulence and reflective speckle, as expressed in the term $f(T_x, R_x, \ldots)$ of Eq. (1), warrants further study. We have also presented simulation results, which are qualitatively consistent with previous experimental observations, of an increase in rms noise with increasing turbulence level. We intend to utilize our simulation of the phenomena involved to conduct further study of the combined effects of reflective speckle and atmospheric turbulence on the lidar method. This methodology is also applicable to a wide range of lidar situations including those involving moving platforms, target albedo variations, wavelength variation effects, and nonuniform turbulence conditions as encountered in systems with slant atmospheric paths.

Appendix A: Modeling of Atmospheric Optical Turbulence

Using the approach of Davis[39] with the Fresnel–Kirchhoff theorem, one can approximate the electric field at an observation point in cylindrical coordinates as[40,41]

$$E(\hat{r}, z) = -\frac{i}{\lambda}\iint_A E(\hat{\rho}, z)\,\frac{\exp[ik(z^2 + |\hat{r} - \hat{\rho}|^2)^{1/2}]}{(z^2 + |\hat{r} - \hat{\rho}|^2)^{1/2}}\,\mathrm{d}A. \tag{A1}$$

Propagation is in the z direction, $\hat{r}$ represents the position vector of the observation point in the x–y plane, and $\hat{\rho}$ is the position vector of the radiating point in the aperture plane. $E(\hat{\rho}, z)$ is the electric field originating in the transmitter aperture of surface area A. It is assumed that the propagation is on axis and paraxial at distances much greater than the wavelength of the laser transmitter ($|\hat{r}| \ll z$ and $|\hat{\rho}| \ll z$). By our approximating the denominator of Eq. (A1) as $(z^2 + |\hat{r} - \hat{\rho}|^2)^{1/2} \approx z$ and using the Fresnel approximation ($|\hat{r} - \hat{\rho}| \ll z$), Eq. (A1) becomes

$$E(\hat{r}, z) \approx -\frac{i}{\lambda z}\int E(\hat{\rho}, 0) \times \exp\left[\frac{i2\pi z}{\lambda}\left(1 + \left|\frac{\hat{r} - \hat{\rho}}{z}\right|^2\right)^{1/2}\right]\mathrm{d}\hat{\rho}. \tag{A2}$$

Expanding the exponential argument and keeping the lowest-order terms, we obtain

$$E(\hat{r}, z) \approx -\frac{i}{\lambda z}\exp\left(\frac{i2\pi z}{\lambda}\right)\int E(\hat{\rho}, 0) \times \exp\left(\frac{i\pi}{\lambda z}|\hat{r} - \hat{\rho}|^2\right)\mathrm{d}\hat{\rho}. \tag{A3}$$

The aperture field can be expanded by use of the FT identity

$$E(\hat{\rho}, 0) = \int \mathrm{d}\hat{f}\exp(2\pi i\,\hat{f}\hat{\rho})\int \mathrm{d}\hat{\rho}' \times \exp(-2\pi i\hat{f}\hat{\rho}')E(\hat{\rho}', 0). \tag{A4}$$

Substituting this identity into approximation (A2) and dropping the term $\exp(i2\pi/\lambda)$, which applies to the entire electric field, we obtain

$$E(\hat{r}, z) \approx -\frac{i}{\lambda z}\int\left[\int \mathrm{d}\hat{f}\exp(2\pi i\hat{f}\hat{\rho})\int \mathrm{d}\hat{\rho}' \times \exp(-2\pi i\hat{f}\hat{\rho}')E(\hat{\rho}', 0)\right]\exp\left(\frac{i\pi}{\lambda z}|\hat{r} - \hat{\rho}|^2\right)\mathrm{d}\hat{\rho}. \tag{A5}$$

Making a change of variables ($\hat{r}' = \hat{r} - \hat{\rho}$) and rearranging, we obtain

$$E(\hat{r}, z) \approx \frac{i}{\lambda z}\int \mathrm{d}\hat{f}\exp(2\pi i\hat{f}\hat{r})\int \mathrm{d}\hat{\rho}' \times \exp(-2\pi i\hat{f}\hat{\rho}')E(\hat{\rho}', 0) \times \left[\int \mathrm{d}\hat{r}'\exp(-2\pi i\hat{f}\hat{r}')\exp\left(\frac{i\pi}{\lambda z}|\hat{r}|^2\right)\right]. \tag{A6}$$

The last integral (in brackets) is the FT of a Gaussian function:

$$\int \mathrm{d}\hat{r}'\exp(-2\pi i\hat{f}\hat{r}')\exp\left(\frac{i\pi}{\lambda z}|\hat{r}'|^2\right) = i\lambda z\exp(-i\pi\lambda z|\hat{f}|^2). \tag{A7}$$

Letting $\hat{\rho}' \to \hat{\rho}$, $E(\hat{r}, z)$ becomes

$$E(\hat{r}, z) \approx \int \mathrm{d}\hat{f}\exp(2\pi i\hat{f}\hat{r}) \times \exp(-i\pi\lambda z|\hat{f}|^2)\int \mathrm{d}\hat{\rho}E(\hat{\rho}, 0)\exp(-2\pi i\hat{f}\hat{\rho}). \tag{A8}$$

Rewritten symbolically,

$$E(\hat{r}, z) \approx \mathrm{IFT}\{\exp(-i\pi\lambda z|\hat{f}|^2)\mathrm{FT}[E(\hat{\rho}, 0)]\}, \tag{A9}$$

where FT is the two-dimensional Fourier transform and IFT is the two-dimensional inverse Fourier transform. This is an expression for the electric

field at a propagation distance z in terms of FT of the electric field at $z = 0$ with $\exp(-i\pi\lambda z|\hat{f}|^2)$ as the Fresnel propagator in frequency space $\hat{f}$.

This research was part of a large lidar project with many important team members, and we thank all of them. In particular we thank Michael Whitehead, Joe Tiee, Chuck Fite, and L. John Jolin for their contributions to this research and in helping us perform these measurements and conduct the simulations. The authors also acknowledge the cooperation of the team at the Nevada Test Site Spill Test Facility. We are very grateful to the project leader, John F. Schultz, who directed this research. This research was fully supported by the U.S. Department of Energy under contract W-7405-ENG-36.

References and Notes

1. R. M. Measures, Laser Remote Sensing: Fundamentals and Applications (Wiley-Interscience, New York, 1984).
2. R. M. Measures, Laser Remote Chemical Analysis (Wiley, New York, 1988).
3. E. D. Hinkley, ed., Laser Monitoring of the Atmosphere (Springer-Verlag, New York, 1976).
4. W. B. Grant, R. H. Kagann, and W. A. McClenny, "Optical remote measurements of toxic gases," J. Air Waste Manage. Assoc. **42,** 18–30 (1992).
5. W. B. Grant, J. S. Margolis, A. M. Brothers, and D. M. Tratt, "CO_2 DIAL measurements of water vapor," Appl. Opt. **26,** 3033–3042 (1987).
6. The reader is encouraged to explore the web site compiled by W. B. Grant on lidar publications at http://w3.osa.org/HOMES/GENERAL/BIBLIO/lidar97.html.
7. E. R. Murray and J. E. van der Laan, "Remote measurement of ethylene using a CO_2 differential-absorption lidar," Appl. Opt. **17,** 814–817 (1978).
8. W. B. Grant, "He–Ne and cw CO_2 laser long-path systems for gas detection," Appl. Opt. **25,** 709–719 (1986).
9. A. Dabas, P. H. Flamant, and P. Salamitou, "Characterization of pulsed coherent Doppler lidar with the speckle effect," Appl. Opt. **33,** 6524–6532 (1994).
10. R. M. Schotland, "Errors in the lidar measurement of atmospheric gases by differential absorption," J. Appl. Meteorol. **13,** 71–77 (1974).
11. S. R. Murty, "Aerosol speckle effects on atmospheric pulsed lidar backscattered signals," Appl. Opt. **28,** 875–878 (1989).
12. V. I. Tatarski, Wave Propagation in a Turbulent Medium, translated by R. A. Silverman (McGraw-Hill, New York, 1961).
13. R. R. Beland, "Propagation through atmospheric turbulence," in *The Infrared Electro-Optical Systems Handbook*, J. S. Accetta and D. L. Shumaker, eds., Vol. PM10 of the SPIE Press Monographs Series (SPIE, Bellingham, Wash., 1993), pp. 157–232.
14. R. L. Fante, "Electromagnetic beam propagation in a turbulent media," Proc. IEEE **63,** 1669–1692 (1975).
15. A. Ishimaru, Wave Propagation and Scattering in Random Media (IEEE Press, New York, 1997).
16. A. Ishimaru, "The beam wave case and remote sensing," in *Laser Beam Propagation in the Atmosphere*, J. W. Strohbehn, ed. (Springer-Verlag, New York, 1978), pp. 129–170.
17. T. Chiba, "Spot dancing of the laser beam propagated through the turbulent atmosphere," Appl. Opt. **10,** 2456–2461 (1971).
18. G. Parry, "Measurement of atmospheric turbulence induced intensity fluctuations in a laser beam," Opt. Acta **28,** 715–728 (1981).
19. D. L. Fried, G. E. Mevers, and M. P. Keister, "Measurements of laser beam scintillation in the atmosphere," J. Opt. Soc. Am. **57,** 787–797 (1967).
20. J. W. Goodman, "Some effects of target-induced scintillation on optical radar performance," Proc. IEEE **53,** 1688–1700 (1965).
21. J. W. Goodman, "Statistical properties of laser speckle patterns," in *Laser Speckle and Related Phenomena*, 2nd ed., J. Dainty, ed. (Springer-Verlag, New York, 1984), pp. 9–75.
22. P. H. Flamant, R. T. Menzies, and M. J. Kavaya, "Evidence for speckle effects on pulsed CO_2 lidar signal returns from remote targets," Appl. Opt. **23,** 1412–1417 (1984).
23. R. R. Petrin, D. H. Nelson, M. J. Schmitt, C. R. Quick, J. J. Tiee, and M. C. Whitehead, "Atmospheric effects on CO_2 differential absorption lidar sensitivity," in *Gas and Chemical Lasers*, R. Sze, ed., Proc. SPIE **2702,** 28–39 (1996).
24. D. H. Nelson, R. R. Petrin, E. P. MacKerrow, M. J. Schmitt, C. R. Quick, A. Zardecki, W. M. Porch, M. C. Whitehead, and D. L. Walters, "Wave optics simulation of atmospheric turbulence and reflective speckle effects in CO_2 differential absorption LIDAR (DIAL)," in *Airborne Laser Advanced Technology*, T. D. Steiner and P. H. Merritt, eds., Proc. SPIE **3381,** 147–158 (1998).
25. E. Durieux and L. Fiorani, "Measurement of the lidar signal fluctuation with a shot-per-shot instrument," Appl. Opt. **37,** 7128–7131 (1998).
26. J. F. Holmes, "Speckle propagation through turbulence: its characteristics and effects," in *Laser Beam Propagation in the Atmosphere*, J. C. Leader, ed., Proc. SPIE **410,** 89–97 (1983).
27. J. H. Churnside, "Aperture averaging of optical scintillations in the turbulent atmosphere," Appl. Opt. **30,** 1982–1994 (1991).
28. M. J. T. Milton and P. T. Woods, "Pulse averaging methods for a laser remote monitoring system using atmospheric backscatter," Appl. Opt. **26,** 2598–2603 (1987).
29. E. P. MacKerrow, M. J. Schmitt, and D. C. Thompson, "Effect of speckle on lidar pulse-pair ratio statistics," Appl. Opt. **36,** 8650–8669 (1997).
30. N. Menyuk, D. K. Killinger, and C. R. Menyuk, "Error reduction in laser remote sensing: combined effects of cross correlation and signal averaging," Appl. Opt. **24,** 118–131 (1985).
31. C. A. Davis and D. L. Walters, "Atmospheric inner-scale effects on normalized irradiance variance," Appl. Opt. **33,** 8406–8411 (1994).
32. J. M. Martin and S. M. Flatté, "Simulation of point-source scintillation through three-dimensional random media," J. Opt. Soc. Am. A **7,** 838–847 (1990).
33. M. Z. M. Jenu and D. H. O. Bebbington, "Intensity scintillation index of finite beam optical propagation in a turbulent atmosphere," Electron. Lett. **30,** 582–583 (1994).
34. M. Tur, "Numerical solutions for the fourth moment of a finite beam propagating in a random medium," J. Opt. Soc. Am. A **2,** 2161–2170 (1985).
35. G. Welch and R. Phillips, "Simulation of enhanced backscatter by a phase screen," J. Opt. Soc. Am. A **7,** 578–584 (1990).
36. D. G. Youmans and G. A. Hart, "Numerical evaluation of the "M" parameter for direct detection ladar," in *Laser Radar Technology and Applications III*, G. W. Kamerman, ed., Proc. SPIE **3380,** 176–187 (1998).
37. H. Fujii, J. Uozumi, and T. Asakura, "Computer simulation study of image speckle patterns with relation to object surface profile," J. Opt. Soc. Am. **66,** 1222–1236 (1976).
38. D. G. Youmans and V. S. R. Gudimetla, "Round-trip turbulence scintillation effects on laser radar: Monte Carlo simulation results for unresolved targets," in *Laser Radar Technology and Applications II*, G. W. Kamerman, ed., Proc. SPIE **3065,** 71–83 (1997).
39. C. A. Davis, "Computer simulation of wave propagation

through turbulent media," Ph.D. dissertation (Naval Postgraduate School, Monterey, Calif., 1994).
40. M. V. Klein and T. E. Furtak, Optics (Wiley, New York, 1986).
41. J. W. Goodman, Introduction to Fourier Optics (McGraw-Hill, New York, 1968).
42. D. L. Knepp, "Multiple phase-screen calculation of the temporal behavior of stochastic waves," Proc. IEEE **71,** 722–737 (1983).
43. J. M. Martin and S. M. Flatté, "Intensity images and statistics from numerical simulation of wave propagation in 3-D random media," Appl. Opt. **27,** 2111–2126 (1988).
44. R. E. Hufnagel, "Propagation through atmospheric turbulence," in *The Infrared Handbook*, W. L. Wolfe and G. J. Zissis, eds. (Environmental Research Institute of Michigan, Ann Arbor, Mich., 1985), pp. 6-1–6-56.
45. J. W. Goodman, Statistical Optics (Wiley, New York, 1985).
46. S. M. Flatté, C. Bracher, and G. Y. Wang, "Probability-density functions of irradiance for waves in atmospheric turbulence calculated by numerical simulation," J. Opt. Soc. Am. A **11,** 2080–2092 (1994).
47. F. G. Gebhard, "High power laser propagation," Appl. Opt. **15,** 1479–1493 (1976).
48. D. L. Fried, "Optical resolution through a randomly inhomogeneous medium," J. Opt. Soc. Am. **56,** 1372–1379 (1966).
49. D. L. Walters, "Atmospheric modulation transfer function for desert and mountain locations: r_0 measurements," J. Opt. Soc. Am. **71,** 406–409 (1981).
50. T. Wang, G. R. Ochs, and S. F. Clifford, "A saturation-resistant optical scintillometer to measure C_n^2," J. Opt. Soc. Am. **68,** 334–338 (1978).
51. H. T. Yura, "Atmospheric turbulence induced laser beam spread," Appl. Opt. **10,** 2771–2773 (1971).
52. W. B. Miller, J. C. Ricklin, and L. C. Andrews, "Log-amplitude variance and wave structure function: a new perspective for Gaussian beams," J. Opt. Soc. Am. A **10,** 661–672 (1993).
53. E. P. MacKerrow and M. J. Schmitt, "Measurement of integrated speckle statistics for CO_2 lidar returns from a moving, nonuniform, hard target," Appl. Opt. **36,** 6921–6937 (1997).
54. J. C. Russ, The Image Processing Handbook (CRC Press, Boca Raton, Fla., 1992).
55. P. R. Bevington and D. K. Robinson, Data Reduction and Error Analysis for the Physical Sciences, 2nd ed. (McGraw-Hill, New York, 1992).